Research Article | Vol. 7, No. 11 | 1 Nov 2016 | BIOMEDICAL OPTICS EXPRESS 4674
Biomedical Optics EXPRESS

Ultrahigh-speed, phase-sensitive full-field interferometric confocal microscopy for quantitative microscale physiology

IKBAL SENCAN,[1,2,7] BRENDAN K. HUANG,[3] YONG BIAN,[1,4] EMILY MIS,[5] MUSTAFA K. KHOKHA,[5] HUI CAO,[6] AND MICHAEL CHOMA[1,3,5,6,8]

[1]*Department of Radiology and Biomedical Imaging, Yale University, New Haven, CT 06520, USA*
[2]*Current affiliation: MGH/HST Athinoula A. Martinos Center for Biomedical Imaging, Department of Radiology, Massachusetts General Hospital, Harvard Medical School, Charlestown, MA 02129, USA*
[3]*Biomedical Engineering, Yale University, New Haven, CT 06511, USA*
[4]*Current affiliation: Department of Otology and Laryngology, Harvard Medical School, Massachusetts Eye and Ear Infirmary, 243 Charles Street, Boston, MA 02114, USA*
[5]*Pediatrics, Yale University, New Haven, CT 06511, USA*
[6]*Applied Physics, Yale University, New Haven, CT 06511, USA*
[7]*isencan@mgh.harvard.edu*
[8]*michael.choma@yale.edu*

Abstract: We developed ultra-high-speed, phase-sensitive, full-field reflection interferometric confocal microscopy (FFICM) for the quantitative characterization of *in vivo* microscale biological motions and flows. We demonstrated 2D frame rates in excess of 1 kHz and pixel throughput rates up to 125 MHz. These fast FFICM frame rates were enabled by the use of a low spatial coherence, high-power laser source. Specifically, we used a dense vertical cavity surface emitting laser (VCSEL) array that synthesized low spatial coherence light through a large number of narrowband, mutually-incoherent emitters. Off-axis interferometry enabled single-shot acquisition of the complex-valued interferometric signal. We characterized the system performance (~2 μm lateral resolution, ~8 μm axial gating depth) with a well-known target. We also demonstrated the use of this highly parallelized confocal microscopy platform for visualization and quantification of cilia-driven surface flows and cilia beat frequency in an important animal model *(Xenopus embryos)* with >1 kHz frame rate. Such frame rates are needed to see large changes in local flow velocity over small distance (high shear flow), in this case, local flow around a single ciliated cell. More generally, our results are an important demonstration of low-spatial coherence, high-power lasers in high-performance, quantitative biomedical imaging.

© 2016 Optical Society of America

OCIS codes: (170.1790) Confocal microscopy; (110.4980) Partial coherence in imaging; (170.3880) Medical and biological imaging; (170.5380) Physiology; (180.3170) Interference microscopy; (250.7260) Vertical cavity surface emitting lasers, Cilia.

References and links

1. D. Psaltis, S. R. Quake, and C. Yang, "Developing optofluidic technology through the fusion of microfluidics and optics," Nature **442**(7101), 381–386 (2006).
2. G. H. Karunamuni, S. Gu, M. R. Ford, L. M. Peterson, P. Ma, Y. T. Wang, A. M. Rollins, M. W. Jenkins, and M. Watanabe, "Capturing structure and function in an embryonic heart with biophotonic tools," Front. Physiol. **5**, 351 (2014).
3. B. K. Huang and M. A. Choma, "Microscale imaging of cilia-driven fluid flow," Cell. Mol. Life Sci. **72**(6), 1095–1113 (2015).
4. A. Zhang, Q. Zhang, C. L. Chen, and R. K. K. Wang, "Methods and algorithms for optical coherence tomography-based angiography: a review and comparison," J. Biomed. Opt. **20**(10), 100901 (2015).
5. H. Zhu and A. Ozcan, "Opto-fluidics based microscopy and flow cytometry on a cell phone for blood analysis," Methods Mol. Biol. **1256**, 171–190 (2015).
6. M. R. Knowles and R. C. Boucher, "Mucus clearance as a primary innate defense mechanism for mammalian airways," J. Clin. Invest. **109**(5), 571–577 (2002).

#272158 http://dx.doi.org/10.1364/BOE.7.004674
Journal © 2016 Received 22 Jul 2016; revised 17 Oct 2016; accepted 17 Oct 2016; published 20 Oct 2016

Biomedical Optics EXPRESS

7. S. H. Randell, R. C. Boucher, "Effective mucus clearance is essential for respiratory health," Am. J. Respir. Cell Mol. Biol. **35**(1), 20–28 (2006).
8. A. Bouwens, D. Szlag, M. Szkulmowski, T. Bolmont, M. Wojtkowski, and T. Lasser, "Quantitative lateral and axial flow imaging with optical coherence microscopy and tomography," Opt. Express **21**(15), 17711–17729 (2013).
9. A. L. Oldenburg, R. K. Chhetri, D. B. Hill, and B. Button, "Monitoring airway mucus flow and ciliary activity with optical coherence tomography," Biomed. Opt. Express **3**(9), 1978–1992 (2012).
10. B. K. Huang, U. A. Gamm, V. Bhandari, M. K. Khokha, and M. A. Choma, "Three-dimensional, three-vector-component velocimetry of cilia-driven fluid flow using correlation-based approaches in optical coherence tomography," Biomed. Opt. Express **6**(9), 3515–3538 (2015).
11. L. Liu, K. K. Chu, G. H. Houser, B. J. Diephuis, Y. Li, E. J. Wilsterman, S. Shastry, G. Dierksen, S. E. Birket, M. Mazur, S. Byan-Parker, W. E. Grizzle, E. J. Sorscher, S. M. Rowe, and G. J. Tearney, "Method for quantitative study of airway functional microanatomy using micro-optical coherence tomography," PLoS One **8**(1), e54473 (2013).
12. J. Lee, W. Wu, J. Y. Jiang, B. Zhu, and D. A. Boas, "Dynamic light scattering optical coherence tomography," Opt. Express **20**(20), 22262–22277 (2012).
13. E. N. Leith, C. Chen, H. Chen, Y. Chen, J. Lopez, P. C. Sun, and D. Dilworth, "Imaging through scattering media using spatial incoherence techniques," Opt. Lett. **16**(23), 1820–1822 (1991).
14. R. H. Webb, "Confocal optical microscopy," Rep. Prog. Phys. **59**(3), 427–471 (1996).
15. R. Chmelik and Z. Harna, "Parallel-mode confocal microscope," Opt. Eng. **38**(10), 1635–1639 (1999).
16. M. G. Somekh, C. W. See, and J. Goh, "Wide field amplitude and phase confocal microscope with speckle illumination," Opt. Commun. **174**(1-4), 75–80 (2000).
17. A. Dubois, L. Vabre, A. C. Boccara, and E. Beaurepaire, "High-resolution full-field optical coherence tomography with a Linnik microscope," Appl. Opt. **41**(4), 805–812 (2002).
18. A. Dubois, K. Grieve, G. Moneron, R. Lecaque, L. Vabre, and C. Boccara, "Ultrahigh-resolution full-field optical coherence tomography," Appl. Opt. **43**(14), 2874–2883 (2004).
19. B. Karamata, P. Lambelet, M. Laubscher, R. P. Salathé, and T. Lasser, "Spatially incoherent illumination as a mechanism for cross-talk suppression in wide-field optical coherence tomography," Opt. Lett. **29**(7), 736–738 (2004).
20. Y. Park, W. Choi, Z. Yaqoob, R. Dasari, K. Badizadegan, and M. S. Feld, "Speckle-field digital holographic microscopy," Opt. Express **17**(15), 12285–12292 (2009).
21. A. Safrani and I. Abdulhalim, "Spatial coherence effect on layer thickness determination in narrowband full-field optical coherence tomography," Appl. Opt. **50**(18), 3021–3027 (2011).
22. T. Slabý, P. Kolman, Z. Dostál, M. Antoš, M. Lošťák, and R. Chmelík, "Off-axis setup taking full advantage of incoherent illumination in coherence-controlled holographic microscope," Opt. Express **21**(12), 14747–14762 (2013).
23. Y. Choi, P. Hosseini, W. Choi, R. R. Dasari, P. T. C. So, and Z. Yaqoob, "Dynamic speckle illumination wide-field reflection phase microscopy," Opt. Lett. **39**(20), 6062–6065 (2014).
24. B. Redding, M. A. Choma, and H. Cao, "Speckle-free laser imaging using random laser illumination," Nat. Photonics **6**(6), 355–359 (2012).
25. B. Redding, Y. Bromberg, M. A. Choma, and H. Cao, "Full-field interferometric confocal microscopy using a VCSEL array," Opt. Lett. **39**(15), 4446–4449 (2014).
26. B. Redding, A. Cerjan, X. Huang, M. L. Lee, A. D. Stone, M. A. Choma, and H. Cao, "Low spatial coherence electrically pumped semiconductor laser for speckle-free full-field imaging," Proc. Natl. Acad. Sci. U.S.A. **112**(5), 1304–1309 (2015).
27. B. Redding, P. Ahmadi, V. Mokan, M. Seifert, M. A. Choma, and H. Cao, "Low-spatial-coherence high-radiance broadband fiber source for speckle free imaging," Opt. Lett. **40**(20), 4607–4610 (2015).
28. S. Knitter, C. G. Liu, B. Redding, M. K. Khokha, M. A. Choma, and H. Cao, "Coherence switching of a degenerate VECSEL for multimodality imaging," Optica **3**(4), 403–406 (2016).
29. S. Jonas, D. Bhattacharya, M. K. Khokha, and M. A. Choma, "Microfluidic characterization of cilia-driven fluid flow using optical coherence tomography-based particle tracking velocimetry," Biomed. Opt. Express **2**(7), 2022–2034 (2011).
30. M. E. Werner, P. Hwang, F. Huisman, P. Taborek, C. C. Yu, and B. J. Mitchell, "Actin and microtubules drive differential aspects of planar cell polarity in multiciliated cells," J. Cell Biol. **195**(1), 19–26 (2011).
31. P. Nieuwkoop and J. Faber, *Normal table of Xenopus laevis (Daudin): a systematical and chronological survey of the development from the fertilized egg till the end of metamorphosis* (Garland Publishing, Inc, New York, 1994).
32. M. A. A. Neil, R. Juskaitis, and T. Wilson, "Method of obtaining optical sectioning by using structured light in a conventional microscope," Opt. Lett. **22**(24), 1905–1907 (1997).
33. E. Auksorius and A. C. Boccara, "Dark-field full-field optical coherence tomography," Opt. Lett. **40**(14), 3272–3275 (2015).
34. K. C. Zhou, B. K. Huang, U. A. Gamm, V. Bhandari, M. K. Khokha, and M. A. Choma, "Particle streak velocimetry-optical coherence tomography: a novel method for multidimensional imaging of microscale fluid flows," Biomed. Opt. Express **7**(4), 1590–1603 (2016).

Biomedical Optics EXPRESS

1. Introduction

Quantifying fluid flow is a major driver of technology development in biomedical imaging. Within the broad field of imaging biomedical fluid flows, optical imaging fills a very important niche in that it is ideally suited to image microscale fluid flows [1–5]. Indeed, there are well-defined yet unmet needs in the optical imaging of microscale fluid flows that drive ongoing technology development. For example, high-speed imaging is needed to monitor flow over large surface areas or to capture fast, time-varying dynamics. The other need is the geometric capability of quantifying transverse fluid flows that are predominantly orthogonal to the optical axis. In the context of coherent, phase-sensitive imaging, relatively mature Doppler technologies are not able to quantify these transverse flows but rather are limited to flow that is parallel to the optical axis.

Cilia-driven flow physiology is an emerging area of biomedical research that would greatly benefit from the ability to quantify transverse flow speeds in a high-speed, cross-sectional manner to better understand the working mechanism of cilia, and to develop clinical screening tools for several diseases due to impaired mucociliary function [3, 6, 7]. Dynamics of flow near cilia themselves, which are beating in the 10-20 Hz range, suggest that frame rates in the 10^2 to 10^3 Hz regime are needed to capture these dynamics. Reflectance mode operation is preferable since transmission-mode operation often is not feasible for imaging flow above thick ciliated specimens. While numerous coherent imaging-based approaches have been developed recently to quantify microscale transverse flows (see, for example, Refs [8–12].), one limitation of these methods is that the scan priority is parallel to the optical axis. That is, image information is collected first along the axis that contains the smallest velocity vector component. As such, for two-dimensional imaging, one of the two transverse directions is not directly imaged. One solution to this limitation is to prioritize scanning in the *en face* plane. While *en face* scanning is feasible with point scanning OCT and confocal microscopy, parallelization of image acquisition to achieve high frame rate flow imaging is more desirable.

Spatial coherence gating is an attractive and scalable approach to achieve full-field *en face* confocal imaging in a parallelized manner. Spatial coherence gating uses full-field, low-spatial coherence interferometry to generate virtual pinholes for transverse localization and axial sectioning [13–23]. That is, interferometric detection of low spatial coherence fields yields a coherent signal that is inherently confocal in the *en face* plane and along the axial dimension. Although the general concept of spatial coherence gating has been described for some time in both narrowband and broadband interferometric imaging, recent advances in low spatial coherence sources make the concept attractive for high-speed (kHz regime) imaging. These advances are yielding light sources that are highly spatially multimode (low spatial coherence) while maintaining high-power per spatial mode [24–28].

Here, we present full-field, cross-sectional imaging of cilia-driven fluid flow physiology in the kilohertz frame-rate regime. We used a dense vertical-cavity surface-emitting laser (VCSEL) array as a narrowband, light source with low spatial coherence for full-field interferometric confocal microscopy (FFICM) that operates in reflection mode. Although each VCSEL emitter has high spatial coherence, combining all the independent emitters together results in a field with relatively low spatial coherence. By using low spatial coherence, off-axis holography, we performed single-shot reconstruction the interferometric signal at very high frame rates. The complex-valued, low spatial coherence interferometric signal is confocal in nature, and can provide information about the backscattered intensity and phase properties of a sample. To demonstrate the potential of high-speed FFICM in ciliary biology, we visualized and quantified fluid flow in the immediate vicinity of a single multiciliated epithelial cell. *En face* imaging showed that predominantly in-plane flow speeds are much faster immediately above the ciliated cell and fall off rapidly as a function of distance away from the cell. Since multiciliated cells are the basic cellular building block of surface flow-generating ciliated surfaces, high-speed FFICM promises to be an important tool

Biomedical Optics EXPRESS

in understanding how patterning of ciliated cells influences bulk flow patterns generated by that surface. More generally, our work is an important demonstration of the potential of low spatial coherence laser sources in massively parallelized cross-sectional optical imaging.

2. FFICM imaging system

Our optical setup (Fig. 1) is an off-axis Linnik interferometer built on an optomechanical cage with two identical aspheric lenses (f = 8 mm, NA = 0.5, Thorlabs, C240TME) at reference and sample arms. The setup is vertically mounted to the optical table through a 1.5”-diameter damped post, such that the sample can be loaded horizontally. The sample holder is placed on a computer-controlled motorized translation stage for axial scanning to acquire confocal z-stacks. The whole reference arm is mounted on a manual translation stage to match its optical path-length to the sample arms, while maintaining the focus on the reference mirror surface, an important design consideration given the non-trivial temporal coherence length of the VCSEL array emission. The illumination unit is composed of a VCSEL array chip (Princeton Optronics, 2 W maximum continuous wave emission, 864 nm center wavelength, ~2 nm FWHM spectral width) mounted on a copper heat sink that is, in turn, mounted on a computer processing unit (CPU) fan to dissipate the excess heat. Emission power is controlled by adjusting the set-point current of a laser diode driver (Thorlabs, LDC240C) operating in constant-current mode. Emission from the 711 elements of the VCSEL array (NA = 0.17) is collected by using an aspheric lens, (f = 11 mm, NA = 0.25) and Köhler configuration is used to illuminate the system. We did not use polarization elements to control the polarization state of the sample illumination. The reflection images of the sample and the tilted reference mirror are then combined at the non-polarizing beam splitter, and magnified by 31.25X (f = 250 mm, ∅ = 25.4 mm) before detected using a high-speed camera (Photonfocus, MV-D1024E-160, Cameralink, 12-bit, 10.6 μm pixel-pitch) with CameraLink board (BitFlow Neon CL). The full active region of the camera (1024x1024 pixels) was used initially for visual inspection and localization of the regions of interests on subjects; a subregion (512x512 pixels, corresponding to a field-of-view of 87 μm by 87 μm on the sample plane) was used for high-speed flow imaging since camera can operate at higher frame rates for reduced number of pixels.

Tilting of the reference mirror enables off-axis holographic retrieval of the complex-valued interferometric signal (Fig. 2). After two-dimensional Fourier transformation of the raw (x, y)-domain signal into the (k_x, k_y)-domain (Fig. 2(b)), the +1st order signal is re-centered around the origin of the (k_x, k_y)-domain and the −1st and 0th order signals are discarded. Subsequent inverse Fourier transformation yields the complex-valued interferometric signal in the (x, y)-domain.

Biomedical Optics EXPRESS

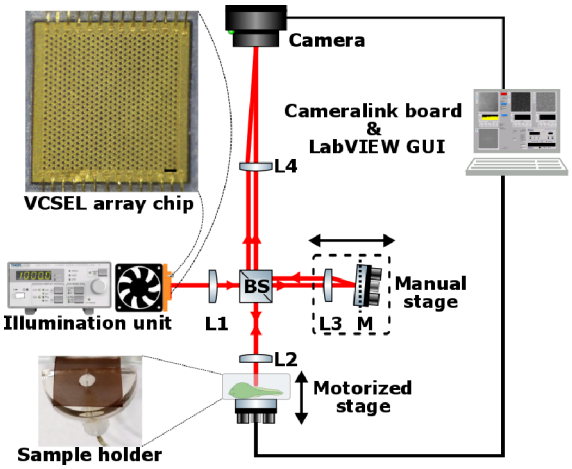

Fig. 1. Full-field interferometric confocal microscopy setup is illustrated. The scale bar on the inset image of the VCSEL array chip is 20 μm long.

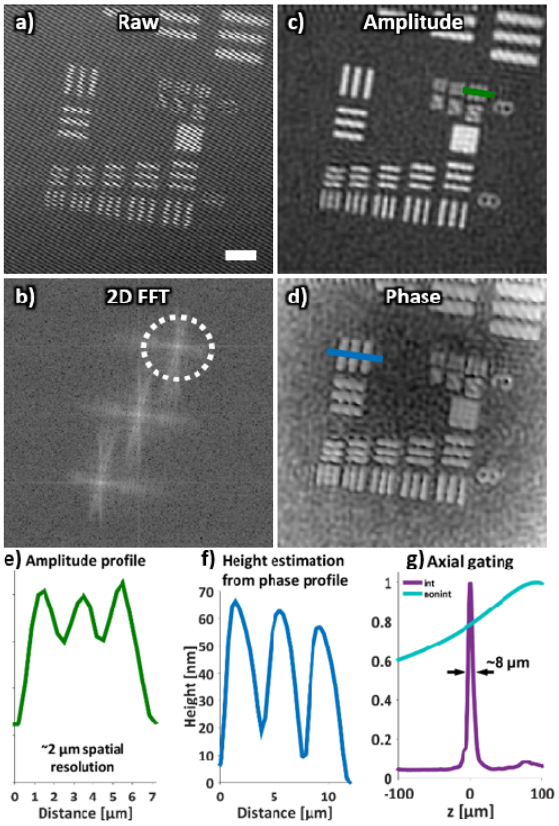

Fig. 2. The amplitude (c) and phase (d) of the complex interferometric signal is retrieved by filtering the 2D spatial Fourier transform (b) of the off-axis raw image (a). The scale bar is 10 μm long. The amplitude profile over the bars (0.98 μm thick) of USAF target ninth group first element (e) suggests the spatial resolution of the system to be approximately 2 μm. Also, the thickness of the chrome coating is estimated from the phase profile (f). The total intensity resulted from noninterferometric and interferometric detection are shown as a mirror is moved through the focus on sample arm. (g) Curves are normalized with the maximum value of each curve. Interferometric detection using VCSEL array provides axial gating (~8 μm) by rejecting out-1of-focus light.

Biomedical Optics EXPRESS

Off-axis holographic reconstruction enables very high speed acquisition without the need for phase stepping. Phase stepping can be challenging to implement in for hundreds of hertz to kilohertz frame-rate imaging. Additionally, even if very rapid phase stepping can be implemented, sample motion needs to be quasi-stationary with respect to a single cycle of phase steps over several image acquisitions in order to prevent fringe wash-out. In contrast, with off-axis holography, sample motion needs to be stationary with respect to the frame integration, which itself can be less than the inverse of the frame rate. Different stages of the off-axis processing as well as confocal microscopic performance are shown in Fig. 2. The in-plane (*x*-*y*) resolution is approximately 2 µm as determined by imaging an Air Force Test Chart with reflective features. The axial resolution is 8 µm. Axial resolution was determined by the full-width half-maximum of the total integrated interferometric (confocal) image intensity as a mirror is axially displaced through focus. Lastly, the phase of the complex-valued signal can be used to estimate the height of sub-resolution axial features.

3. Ultrahigh speed FFICM imaging of ciliary physiology

We next used FFICM to quantify ciliary physiology in *Xenopus* embryos (tadpoles). The epithelium (skin) of *Xenopus* embryos is ciliated and generates a head-to-tail flow. The epithelium is not continuously ciliated. Rather, multiciliated cells are separated by approximately 20 to 100 µm across the epithelium. Lower resolution imaging does not have sufficient resolution to quantify fluid flow in the immediate vicinity of a single multiciliated cell. Additionally, frame rates need to be sufficiently fast to capture ~1 mm/s flows at few micrometer spatial resolution. Indeed, in our experience using OCT (*x*-*z* plane) imaging in the ~10 µm resolution suggests that flow near the surface is ~1 mm/s, but out-of-plane motion prevents full capture of this motion. In order to demonstrate the confocal nature of FFICM in *Xenopus* ciliary biology, we acquired a *z*-stack of images (Fig. 3(a)-3(c)), starting near the surface of the embryo by using 5 µm diameter polystyrene beads (Bangs Laboratories, Fishers, IN, USA). In this *z*-stack, the skin has a pigmented cell that generates a high level of backscatter (Fig. 3(a)). Although ciliated cells also generate significant backscatter, a pigmented cell can be distinguished from a ciliated cell based on the time-varying nature of the backscattered signal. As discussed below, the scattering signal from a ciliated cell changes in time at a frequency consistent with the ciliary beat frequency. On the other hand, pigmented cell scattering is static in time. Moving further above the surface of the embryo, tracer particles move at a speed that decreases with increasing distance from the surface, consistent with prior results [29]. By generating maximum projection images over some time interval Δt, particle speed can be estimated by taking the quotient of the manually-estimated particle streak length Δs and Δt.

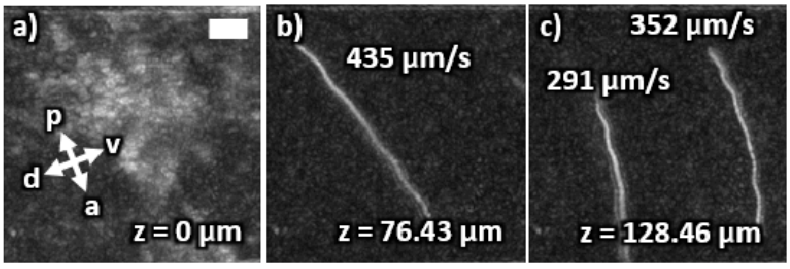

Fig. 3. Maximum intensity projection images over 2.43ms, 250 images at different heights from a pigmented region on the Xenopus skin, z = 0 µm (a), 76.43 µm (b), and 128.46 µm (c) are reported to show the change in flow profile as a function of depth. Data acquisition frequency is 1380.26 Hz. The scale bar is 10 µm long. The field of view is 87 µm by 87 µm (512x512 pixels). Visualization 1 has the same FOV. a, anterior (towards the head); d, dorsal; p, posterior (towards the tail); v, ventral.

Biomedical Optics EXPRESS

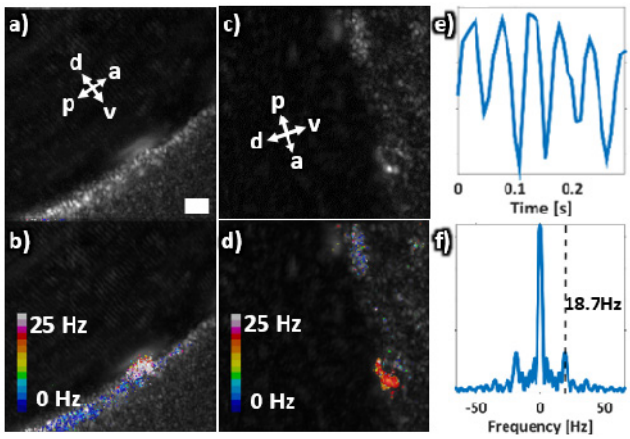

Fig. 4. The standard deviation images (a and c, grayscale) are overlaid with the dominant frequency maps (b and d, 16-color) over two ROIs on different tadpoles. Note how the spatial distributions of the dominant frequencies overlap with ciliated regions that are in focus. The intensity fluctuations from one pixel within the anterior ciliated region of (c) is plotted as an example (e). The Fourier transform of this signal (f) peaks at 18.7 Hz, which corresponds to the measured cilia beating frequency at this location. The scale bar is 10 μm long. The field of view is 87 μm by 87 μm (512x512 pixels).

Given our high frame rate, we next analyzed the time-varying interferometric intensity signal. In particular, we analyzed the Fourier transform of intensity versus time signal at each spatial pixel in time series acquisition. Regions that morphologically are consistent with multiciliated cells on speckle variance imaging have frequency peaks in the ~18-25 Hz range, consistent with prior work in direct, high-speed visualization of *Xenopus* embryo cilia [30]. In Fig. 4, we show the beat frequency map over the same region-of-interests (ROI), for which we reported the spatial velocity at the proximity of multiciliated cells in Fig. 5 and Fig. 6. The dominant frequency values are computed for each pixel by first taking the Fourier transform along the time axis and normalizing it with the average spectrum of all the pixels to remove the background movement. After we apply a 30% threshold and bandpass filtering in the frequency range from right above 0 Hz up to 27 Hz to remove the DC and its harmonics, we detected dominant frequency, where the maximum peak is located in the spectrum.

For flow near the cilia, it is reasonable to assume that, given low Reynolds number physiology, the fluid moves in approximate lockstep with the tips of the cilia. Using this assumption, the duration of the power stroke can be approximated. If the average speed during the ciliary power stroke is 1.5 mm/s and if the power stroke distance is 20 μm, the power stroke duration is 13 ms. If the beat frequency is 20 Hz, the recovery stroke duration is 37 ms. These estimates yield a time ratio of the recovery time and the power stroke time of 2.8, which is consistent with estimating the ratio from direct visualization of ciliary motion in Ref [30].

Biomedical Optics EXPRESS

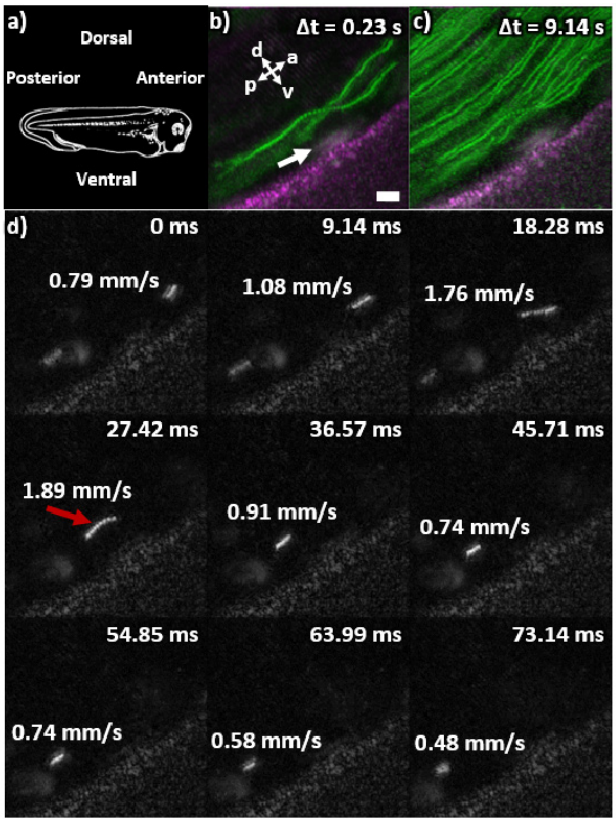

Fig. 5. The cilia-driven flow on Xenopus tropicalis embryo (same ROI as Fig. 4a-b) at Nieuwkoop-Faber stage [31] early 30s (a) is analyzed with FFICM setup. Standard deviation image over time (magenta) emphasizes the skin boundary and structures. The white arrow marks a region with multi-ciliated cells. This standard deviation image is overlaid with maximum intensity projection (green) images over 0.23 s, 250 frames (b) and 9.14 s, 10,000 frames (c) to emphasize the flow profile over the skin. A nine-image montage (d) is showing the movement of a bead over the multi-ciliated cells. The white strike that shows the bead path (red arrow) gets longer as the bead moves faster around the cilia patch. The speed of the particle on the image plane is calculated by dividing the traveled path to the total time. Each image is the maximum intensity projection of 10 frames. The scale bar is 10 µm long. The field of view is 87 µm by 87 µm (512x512 pixels). Visualization 2 has the same FOV. The acquisition frame rate is 1,093.85 Hz.

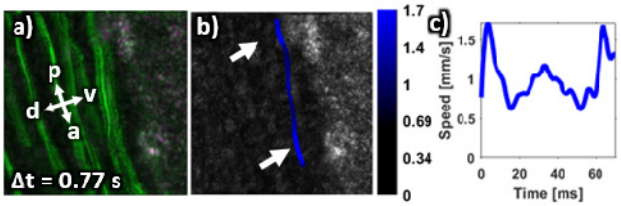

Fig. 6. The cilia-driven flow on a tadpole embryo (same ROI as Fig. 4(c)-4(d)) at stage early 40s is quantified. Standard deviation image (magenta) is overlaid with maximum intensity projection (green) image (over 0.77 s, 1000 frames) (a) to emphasize the flow profile over the skin. Posterior ciliated region is slightly out-of-focus. The total speed on the *en-face* plane for one bead is shown over its trajectory (b). Two white arrows mark the areas with multi-ciliated cells. The speed vs. time graph (c) clearly shows how the bead speed up in the proximity of the ciliated region. The field of view is 87 µm by 87 µm (512x512 pixels). Visualization 3 has the same FOV. Data acquisition frequency is 1,308.04 Hz.

Biomedical Optics EXPRESS

4. Discussion and conclusion

Overall, there is a lack of methods that can, in reflection mode, image and quantify near-field cilia driven fluid flow generated by an individual multiciliated cell over the course of a single beat cycle (Visualization 4; the FOV of each panel is 87 μm by 87 μm). Ultrahigh speed FFICM addresses this gap. Here, we define "near-field" as being within about one cilia length (~10-20 μm). Individual multiciliated cells are the building blocks of ciliated surface. Understanding the performance of this individual unit is an important step in understanding the flow generated by the collective action of many ciliated cells. The ciliated skin of *Xenopus* embryos is an intriguing model for studying both individual and collective action of cilia. Specifically, the skin is relatively sparsely ciliated, with multiciliated cells separated by ~20 to 100 μm. Thus, ciliated cells are largely far-field with respect to each other.

Based on the length of the cilia and the ciliary beat frequency, the tip of the cilia is expected to have a peak speed on the order of 1 mm/s. The rationale for the ~1 mm/s speed is as follows. For a ciliary beat frequency of ~15 Hz, the beat period is 67 ms. The duration of the power stroke (the portion of the beat that is responsible for generating directed flow) is less than the duration of the recovery stroke. As such, it can be assumed that the power stroke duration is no more than ~30 ms. If it is assumed that a cilium traces out a semicircle over the course of the power stroke, and if it assumed that the radius of that semicircle is 10 μm, then the length of that semicircle is πr~30 μm. The average speed of the cilia tip is thus no slower than ~(30 μm)/(30 ms)~1 mm/s. Based on no-slip boundary conditions, the fluid in contact with the tip of the cilia would move at the same velocity as the tip of the cilia itself. Likewise, the near-field flow speeds would be expected to be ~1 mm/s. Our imaging using the >1 kHz frame rate confirms that the near-field flow speeds are indeed in this regime. Surface imaging near a ciliated cell using FFICM also shows that the flow speeds rapidly drop off when moving from the near-field to the far-field. These large spatial variations in surface flow speeds (relatively high-shear speed changes of ~1 mm/s over ~10 μm ranges) are inaccessible to slower-speed, lower resolution OCT imaging that we previously have performed. Indeed, flow speeds near the skin are not spatially smooth while flow further away from the skin is indeed spatially smooth. Surface flow is not smooth because it is a combination of near-field flow and far-field flow. Flow more than a few tens of microns away from the skin is purely far-field.

It also is worth noting that imaging speed is an important consideration in the general feasibility of coherent full-field methods that employ interferometry. To that point, the present work represents an orders-of-magnitude improvement in the application of a specific theoretical concept, that is, the use of low spatial coherence to enable massively parallel confocal microscopy. If there is significant particle motion over the camera integration period, then the camera will integrate over a significant portion of an interferometric fringe which will, in turn, significantly decrease the visibility or contrast of the interferometric signal. For an imaging wavelength of ~800 nm operating in reflection mode (double-pass mode), axial motion of a few hundred nanometers would significantly reduce fringe visibility, leading to significant confocal signal attenuation. For this reason, imaging in the >1 kHz frame rate regime is important. We also note that, for similar reasons relating to interferometric fringe visibility when performing *in vivo* imaging, operating in the >1 kHz line rate regime was critical to the success of spectrometer-based Fourier domain OCT.

The imaging system presented here exploits the fact that interferometric detection of low spatial coherence fields yields a coherent signal that is inherently confocal in the transverse plane and along the axial dimension. An alternate framing of the mechanisms of confocality through interferometric detection of low spatial coherence fields is as follows. A scanning laser microscope that uses a single-mode source can be made confocal without using a detector pinhole through interferometric detection of the backscattered light on a 2D camera [14]. That is, the interferometric signal is fully confocal. Instead of scanning the beam, imaging at multiple lateral positions can be accomplished by adding more single-mode

Biomedical Optics EXPRESS

emitters to the source (i.e. synthesize an extended low spatial coherence source from many single-mode sources). In this framing, the low spatial coherence is a consequence of using spatial multiplexing to perform highly parallelized confocal microscopy. We also note that the evidence suggests that the one-to-one relationship between source spatial mode and images resolution element can be relaxed at low to moderate levels of scattering [19, 25].

Imaging speed also is an important consideration when considering modulation schemes that are required to generate and recover a full-field confocal signal. Off-axis holography has the advantage of single-shot acquisition, which is a major advantage when imaging fast biological events such as near-field cilia-driven fluid flow. On the other hand, some other coherent (e.g. phase-stepping [17]) and incoherent (e.g. structured illumination for confocal-type cross-sectional imaging [32]) approaches require the acquisition of three or more images taken at different modulation states. The reconstruction process in both phase-stepping interferometry and structured illumination assumes that the imaged object is stationary over the course of the three (or more) image acquisitions. In the case of flow imaging using flow tracers, the tracer particles need to have minimal motion over the multiple raw image acquisitions. In our results, there was clear inter-frame motion of tracer particles near cilia when imaging at ~1 kHz frame rates. As such, structured illumination would require switching between grid patterns at a rate much faster that 1 kHz, which is very challenging from a technical perspective. It also places an increased demand on camera readout rates since frame rate needs to match the pattern switch rate. While there are methods for simultaneous acquisition of raw images as a multiplicity of grid patterns, we would argue that these systems are no simpler if not more complicated than off-axis holography.

In a prior work, we used a multimode fiber to deliver light from the VCSEL array to the sample [25]. In this work, we used bulk-optic Köhler illumination. Our rationale for removing the multimode fiber (MMF) and using bulk-optic Köhler illumination is as follows. The optical field resulting from the combination of the many VCSEL emitters has low spatial coherence. When propagated through multimode fiber, the resultant field has a speckle contrast of a few percent. Although this low degree of speckle contrast is difficult for a human eye to detect, the low speckle contrast is nevertheless captured by a digital camera. As such, the sample illumination photon statistics are no longer driven by the underlying (presumably Poisson) photon statistics of the emitters but rather by the statistics of low-contrast speckle. Put another way, sample illumination with low contrast speckle (generated by propagation of a low spatial coherence field through MMF) results in a variation in sample illumination intensity of a few percent, which can be thought of as the spatial analog of (temporal) intensity noise in point-scanning microscopy. In order to avoid this intensity noise, we opted to use Köhler illumination, which yields sample illumination that is nominally uniform and non-speckled.

Although full-field interferometric detection of low-coherence light can enable confocality, it is prone to some artifacts that are not present in point-scanning, direct-detection reflection confocal microscopy. Unlike point-scanning methods that use physical pinholes to reject stray light (e.g. specular reflections off of lenses and beamsplitters, ghost images of the sample from multiple reflections), full-field methods collect stray light and computationally reject it. Our source has an effective speckle contrast of a few percent. We attribute the static background speckle to the stray light that generates speckle and diffraction artifact. The speckle has a nominal center spatial frequency centered at the passband of the band-pass filter used in off-axis processing. We note that future iterations of the demonstrated imaging system may employ dark-field approaches [33] to physically mitigate stray light.

Lastly, we note some limitations of the demonstrated FFICM system. As with other 2D imaging modalities, particle tracking capabilities are limited by particles moving out-of-plane, although we note that in-plane dwell time contains information about out-of-plane speed [34]. We used physical mirror-tilt (spatial group delay gradient) in the reference arm to generate off-axis fringes. Had we not limited the camera readout field-of-view in order to increase

Biomedical Optics EXPRESS

frame rate, we may have observed decreased spatial mode overlap further away from the center of the field-of-view due to defocus of the reference modes. We were able to use physical tilt and not a grating (spatial phase delay gradient; see, for example [22],) since we used a monochromatic source. Likewise, since we read out only the center portion of the illuminated field-of-view, we limited the presence of aberrations in our images that may be generated by our use of an aspheric lens. The imaging performance of FFICM is to some extent limited by the performance of current-generation cameras. Despite high frame rates, well depth is limited and, in turn, limits imaging dynamic range. This is one of the paradoxes of parallelization: it requires longer integration times in order to capitalize on multiplexing, which pushes hardware requirements. Nonetheless, we believe that full-field approaches show promise towards implementing ultra-high frame imaging to interrogate novel physiological function.

Funding

This work is supported by the National Institutes of Health (NIH) (1R21EB016163-01A1,1R01HL118419-01,1R21HL125125-01A1); Office of Naval Research (ONR) (MURI N00014-13-1-0649).

130.132.173.130 {ts '2016-12-29 17:43:18'}